APPLIED ORIGAMI

Using origami design principles to fold reprogrammable mechanical metamaterials

Jesse L. Silverberg,[1]* Arthur A. Evans,[2] Lauren McLeod,[1] Ryan C. Hayward,[3] Thomas Hull,[4] Christian D. Santangelo,[2] Itai Cohen[1]

Although broadly admired for its aesthetic qualities, the art of origami is now being recognized also as a framework for mechanical metamaterial design. Working with the Miura-ori tessellation, we find that each unit cell of this crease pattern is mechanically bistable, and by switching between states, the compressive modulus of the overall structure can be rationally and reversibly tuned. By virtue of their interactions, these mechanically stable lattice defects also lead to emergent crystallographic structures such as vacancies, dislocations, and grain boundaries. Each of these structures comes from an arrangement of reversible folds, highlighting a connection between mechanical metamaterials and programmable matter. Given origami's scale-free geometric character, this framework for metamaterial design can be directly transferred to milli-, micro-, and nanometer-size systems.

Metamaterials are rapidly emerging at the frontier of scientific and technological innovation due to their exotic and tunable material properties, which arise from arrangements of smaller units within the bulk system (*1*–*5*). Once fabricated, structural modifications are generally difficult, making it rare to find metamaterials that can be reconfigured beyond their original design. Origami-inspired mechanical metamaterials offer enhanced flexibility in performance because their properties are coupled to a dynamically alterable folding pattern (*6*–*16*). Hence, multiple stable configurations can manifest from a single structure yielding programmable metamaterials.

We studied the Miura-ori tessellated folding pattern, which has recently been proposed as an origami metamaterial (Fig. 1, A to C, figs. S1 to S3, and movie S1) (*14*, *15*). Historically, this design was invented to efficiently pack solar panels for space missions (*17*), but the morphology also naturally occurs in leaves (*18*) and embryonic intestine (*19*, *20*) and generally arises when thin sheets tethered to a surface undergo biaxial compression. The geometry of a Miura-ori is a herringbone pattern that emerges from a series of convex mountain and concave valley creases (Fig. 1C). Vertices are formed when four creases intersect, and four adjacent vertices bound equal-area facets arranged with inversion symmetry (Fig. 1B). This fold pattern defines a lattice characterized by two static crease lengths ℓ_1, ℓ_2, and one static plane angle α. To quantify folding, a vertex angle ε is required (Fig. 1C); when $\varepsilon = 180° - 2\alpha$, the structure is maximally contracted into a folded state, and when $\varepsilon = 180°$, the structure is an unfolded flat sheet.

If folded from an ideal material with infinite stretching modulus, the Miura-ori would have only one degree of freedom described by ε (*14*). However, generating samples from laser-cut sheets of paper and mylar (Fig. 1C) (see supplementary materials for details), we find additional degrees of freedom, as evidenced by soft bending modes (*14*, *15*). As an extreme example, the Miura-ori supports highly localized heterogeneity introduced after folding by applying force to a vertex in the normal direction and popping it into a categorically different mechanically stable state (Fig. 2A, fig. S4A, and movie S2). This pop-through defect (PTD) changes lattice topology by suppressing one fold and bending adjacent facets through an angle ϕ (Fig. 2, B and C). Quantifying lattice distortion by the surface's Monge patch mean curvature calculated from three-dimensional (3D) digitized scans, we find that displacements of vertices in the xy plane are negligible within a distance of one unit cell; this compares favorably with theoretical predictions that estimate a distortion decay length ≈1/2 the unit cell width (Fig. 2D) (see supplementary materials for details) (*21*, *22*). Although highly localized, PTDs are unlike conventional lattice defects because they involve only elastic facet bending and hence are reversibly removable.

To determine the robustness of PTDs to mechanical perturbations, we theoretically model a single unit cell with one mountain and three valley folds in mechanical equilibrium (similar to the paper model in Fig. 2, B and C). To account for experimentally observed facet bending, two additional symmetrically placed creases are included whose folding angles ϕ are equal and have equilibrium values of 180° (*14*, *15*). We assume a Hookean energy expression for all creases and calculate the dimensionless energy u as a function of the folding configuration (Fig. 2E and fig. S5) (see supplementary materials for details). We observe that the energy landscape has two distinct regions, each with its own local minimum (Fig. 2E, points I and II), that are connected at a single point corresponding to a fully unfolded unit cell where $\phi = \varepsilon = 180°$. For materials with a finite stretching modulus, this connecting point widens along the ϕ axis and allows for otherwise forbidden stretching-enabled transitions. Because the stretching modulus is proportional to sheet thickness (*23*), the energy required to transition between states is a tunable design feature. Thus, while PTDs are introduced reversibly, their stability to mechanical perturbations is controlled by the competition between the material's bending and stretching energy scales.

The mechanical consequences of a PTD were determined by folding laser-cut structures from 24-lb paper with s^2 unit cells, where s was varied from 3 to 8 and α was fixed at 60°. A centrally located defect was introduced by hand, and the compressive modulus $K_y^{\text{defect}}(\varepsilon)$ was measured as a function of defect density $n = 1/s^2$ (see supplementary materials for details). Normalizing these data by the modulus of a defect-free lattice, $K_y^{\text{normal}}(\varepsilon)$, revealed a divergence in stiffness as a function of compression limited only by tearing of the sheet at the highest strains (Fig. 2F and fig. S4B). This divergence arises from a violation of Maekawa's theorem, which requires the number of mountain folds minus the number of valley folds at every vertex to be ±2 for a structure to fold flat (*24*). By linking enhanced mechanical stiffness to violations of a canonical paper-folding theorem, these data experimentally demonstrate how geometric constraints in origami-based design can dominate bulk material properties.

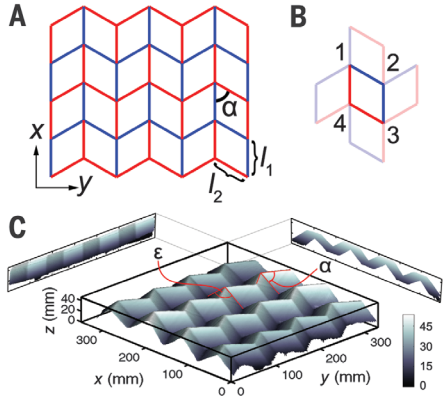

Fig. 1. Schematic and 3D reconstruction of the Miura-ori with definition of important geometric parameters. (**A**) The Miura-ori crease pattern on a flat sheet is depicted with alternating mountain (red) and valley (blue) folds. (**B**) Each facet is bounded by four vertices labeled 1 through 4. (**C**) An experimentally recorded 3D image of a 4 by 4 laser-cut Miura-ori with two in-plane projections shows the folded structure at equilibrium. The color bar gives height in mm.

[1]Physics Department, Cornell University, Ithaca, NY 14853, USA. [2]Department of Physics, University of Massachusetts, Amherst, MA 01003, USA. [3]Department of Polymer Science and Engineering, University of Massachusetts, Amherst, MA 01003, USA. [4]Department of Mathematics, Western New England University, Springfield, MA 01119, USA.
*Corresponding author. E-mail: JLS533@cornell.edu

Nevertheless, such constraints are still malleable; the value of ε where K_y^{defect} increases is shifted simply by varying n. Thus, PTDs make attractive elements for metamaterial design because the onset and strength of K_y^{defect} are rationally tunable, and moreover, these "mechanical pixels" can be activated on demand to vary the bulk compressive properties. Although PTDs were manually introduced here, soft robotics-based technology (*25*), microelectromechanical systems actuator arrays (*26*), or even thermal fluctuations (*27*), provide alternative avenues to introduce and remove PTDs.

To understand both the density dependence and compression dependence of the Miura-ori with a PTD, we analytically calculated the intrinsic PTD compressive modulus, K_y^{PTD} (see supplementary materials for details). This was found by noting that the stress a PTD exerts is proportional to its extension relative to the neighboring undefected unit cells. At low defect densities for a lattice of arbitrary size, the compressive modulus of a lattice with a PTD can be expressed in a dipole expansion, $K_y^{defect} = K_y^{normal} + nK_y^{PTD}$, where K_y^{PTD}

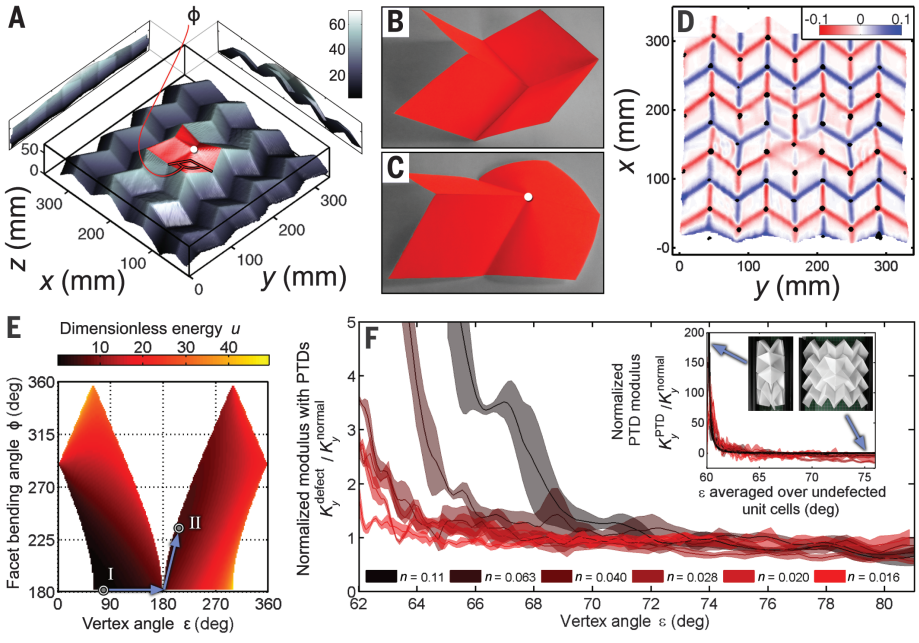

Fig. 2. Experimental data showing spatial confinement of a PTD and combined experimental/theoretical data for PTD mechanics. (**A**) 3D reconstruction of a Miura-ori with a centrally located PTD (red facets). The color bar is height in mm. (**B**) Photograph of a single vertex shows that it is mechanically stable in isolation, as is a PTD (**C**). (**D**) Mean curvature of 3D scan from (A) shows a modified crease pattern in the presence of a PTD. The color bar is in units of mm^{-1}. Overlapping vertex position of same lattice without a PTD (black dots) shows that the PTD is highly localized and causes minimal distortion in finite-sized lattices. (**E**) Theoretical energy diagram of a single vertex has two energy minima corresponding to a (I) normal and (II) PTD state. Arrows indicate direct pathway to PTD formation. The white background is geometrically forbidden. (**F**) Experimentally measured modulus as a function of compression ε and PTD density n. (Inset) Data follow a theoretically predicted scaling collapse (black line).

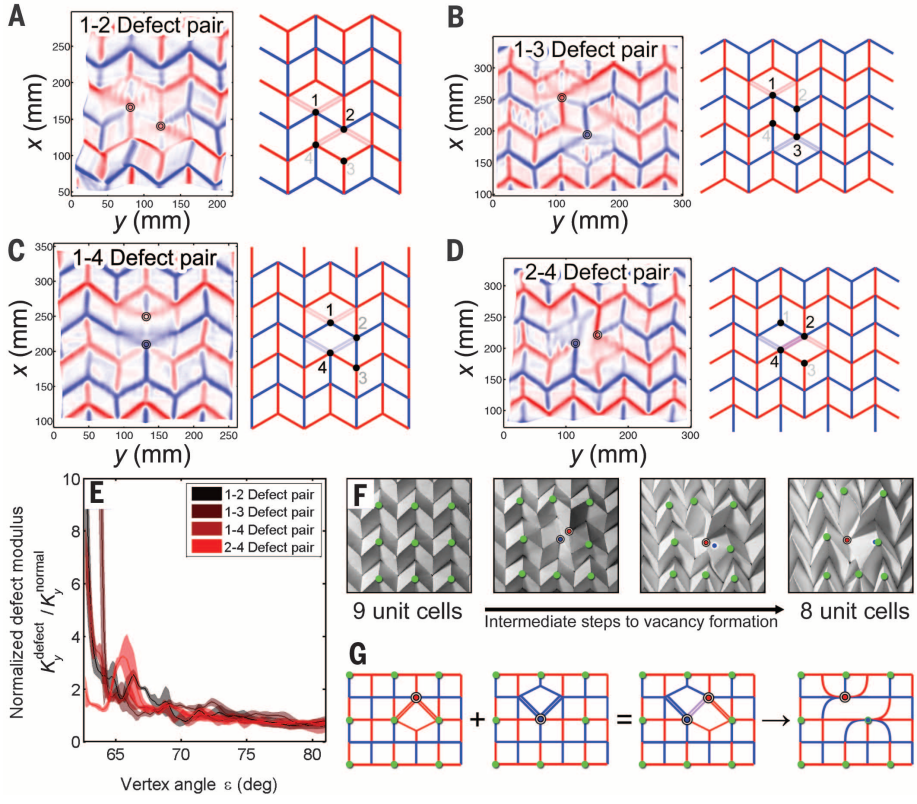

Fig. 3. Experimental data of two interacting PTDs. Mean curvature maps of (**A**) 1–2, (**B**) 1–3, (**C**) 1–4, and (**D**) 2–4 defect-pair configuration. The color maps saturate at ±1 mm^{-1}. Schematic diagrams show defect placement (dots) and facet bending (double lines). (**E**) Normalized compressive modulus of lattice with each defect-pair configuration shows that three combinations lead to divergent stiffness, whereas the 2-4 configuration does not. (**F**) Labeling nine unit cells with green dots and examining their location as ε decreases demonstrates how the 2–4 defect configuration (red and blue dots) leads to a lattice vacancy. (**G**) Schematic diagrams show where defects interact and the resultant crease pattern.

is a function of ε averaged over the nondefected unit cells. This expression is valid when $n << 1$ and holds for a lattice with multiple defects as long as defect interactions can be neglected. Moreover, it suggests a data collapse with a one-parameter fit to the theory that sets the scale of K_y^{PTD}. Indeed, we find such a collapse (Fig. 2F, inset) and excellent agreement with the analytic expression (Fig. 2F, inset, black line), demonstrating that the contribution of PTDs to the modulus at low densities is linearly additive. This mechanical response is useful for design purposes because it offers great simplicity in predicting the compressive modulus of a Miura-ori with PTDs.

With increasing density, PTD interactions become important, particularly when pairs of defects are on adjacent vertices. There are four unique defect pairs: 1–2, 1–3, 1–4, and 2–4, with the other combinations degenerate by symmetry (Fig. 1B and Fig. 3, A to D). Folding 4 by 4 lattices with $\alpha = 60°$, we measured $K_y^{defect}(\varepsilon)$ in the presence of the four unique defect pair configurations. Normalizing by the defect-free modulus, we found that the 1–2, 1–3, and 1–4 defect pair moduli diverge as the compression increases (Fig. 3E and movie S3).

Surprisingly, the 2–4 configuration has qualitatively different compressive behavior: The modulus first increases during compression similar to other defect-pair configurations, but then decreases, and finally reduces to a near defect-free value at the highest compressions (Fig. 3E). Effectively, the respective mechanical signatures of the 2–4 defect pair are annihilated during compression. To illustrate the folding sequence, we mark the centers of a 3 by 3 sublattice (Fig. 3F, green dots), as well as the location of each defect (Fig. 3F, red and blue dots). During compression, facets near the defect sites are increasingly bent as ε decreases, leading to the enhanced stiffness. This enhancement progresses until defect site 4 folds under defect site 2 and all four creases on the facet flip. The defect sites then collapse onto, and overlap with, nearby vertices (Fig. 3F) so that the center lattice site is tucked underneath the adjacent unit cell (movie S4). Visually inspecting the 2–4 defect pair reveals a notable consequence: This defect configuration generates a lattice vacancy analogous to those seen in crystallographic systems (*28*).

To understand why the 2–4 defect pair is special, we compute the mean curvature from 3D scans of laser-cut sheets (Fig. 3, A to D). Comparing the four cases, we see that the 2–4 pair is distinguished by overlapping bending facets of equal magnitude but opposite sign, as quantified by the zero mean curvature on the central facet. This cancellation is possible due to the symmetry of the 2–4 placement and the reversibility of a PTD's deformation of a Miura-ori lattice. When fully compressed, the defect-modified crease pattern is compatible with Maekawa's theorem for flat-foldability (Fig. 3G and fig. S6), and hence the compressive modulus is restored to a nearly defect-free value.

Recognizing the 2–4 defect pair as a lattice vacancy immediately suggests that the Miura-ori supports other types of crystallographic defects (*23*). For example, a column of vacancies forms an edge dislocation (Fig. 4A), and several adjacent edge dislocations form a grain boundary (Fig. 4B). In both cases, these reconfigurations of the lattice are flat-foldable; however, non–flat-foldable configurations are possible as well. For example, a column of PTDs on alternating vertices generates a hinge-like structure that allows the Miura-ori to easily bend out of plane (Fig. 4C). Conversely, a column of PTDs on consecutive vertices forms a corrugated structure that is highly resistive to out-of-plane bending (Fig. 4D). In fact, rationally introducing patterns of defects as design elements swiftly generates a vast library of origami-inspired mechanical metamaterials. To demonstrate in experiments the ability to place these features without permanently altering the crease pattern, we programmed eight configurations into a single sheet with 13 consecutive reprogramming events (Fig. 4E) (*29*). Measuring $K_y^{programmed}$ for a lattice compressed to 68% of its initial width, we found that once calibrated (dashed lines), we are able to predict and realize target modulus values when defect concentration and interactions are altered (solid black lines). This capability to dynamically reprogram elastic properties illustrates the power of our approach.

Extending programmable metamaterial design principles to self-folding robotic (*25*, *30*–*33*) and polymer (*8*–*10*, *13*, *16*) systems opens the door to engineering devices that can alter their mechanical functionality on demand. Such enhanced capabilities would move these transforming systems whose function depends on configuration from what was merely science fiction in past decades to real-world applications.

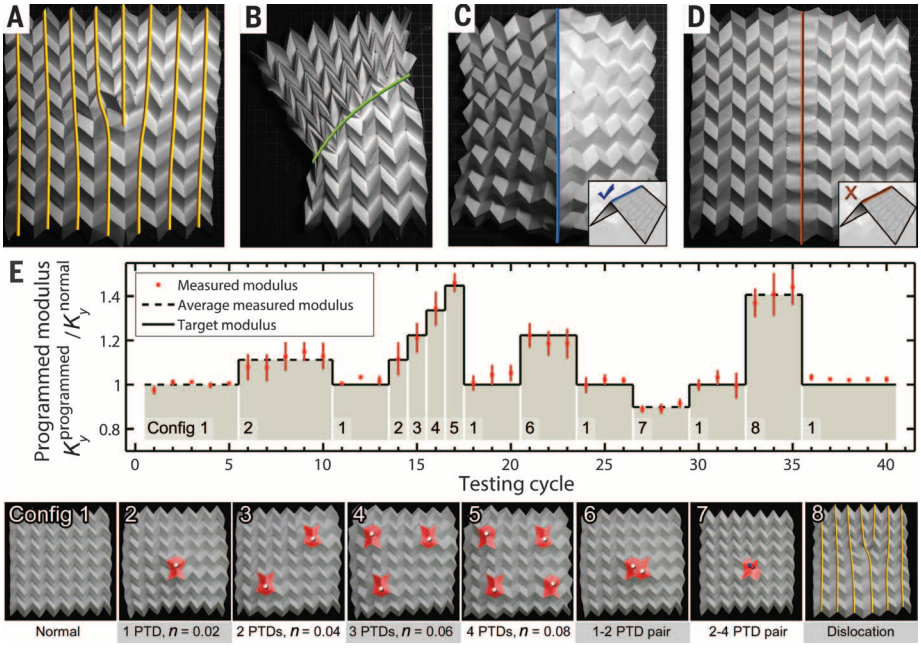

Fig. 4. Photographs of a Miura-ori with complex defect structures and experimental demonstration of a programmable modulus. (**A**) Column of lattice vacancies (2–4 pairs) generate an edge dislocation. (**B**) Columns of edge dislocations generate a grain boundary. (**C**) Column of PTDs on alternating vertices behaves like a hinge. (**D**) Column of PTDs on consecutive vertices generates rigid corrugated structure. (**E**) Experimentally measured modulus over 40 testing cycles with eight distinct configurations and 13 reprogramming events. Dashed lines are averages of measured values (red dots) and are used to generate predicted target values of the modulus (solid lines). Data demonstrate reversibility and programmability. Photographs below the plot show corresponding structure, with PTDs highlighted as a guide for the eye.

REFERENCES AND NOTES

1. M. Wegener, *Science* **342**, 939–940 (2013).
2. Y. Liu, X. Zhang, *Chem. Soc. Rev.* **40**, 2494–2507 (2011).
3. J.-H. Lee, J. P. Singer, E. L. Thomas, *Adv. Mater.* **24**, 4782–4810 (2012).
4. A. Q. Liu, W. M. Zhu, D. P. Tsai, N. I. Zheludev, *J. Opt.* **14**, 114009 (2012).
5. M. Kadic, T. Bückmann, R. Schittny, M. Wegener, *Rep. Prog. Phys.* **76**, 126501 (2013).
6. C. Py *et al.*, *Phys. Rev. Lett.* **98**, 156103 (2007).
7. A. Papa, S. Pellegrino, *J. Spacecr. Rockets* **45**, 10–18 (2008).
8. N. Bassik, G. M. Stern, D. H. Gracias, *Appl. Phys. Lett.* **95**, 091901 (2009).
9. J. Kim, J. A. Hanna, M. Byun, C. D. Santangelo, R. C. Hayward, *Science* **335**, 1201–1205 (2012).
10. J. Kim, J. A. Hanna, R. C. Hayward, C. D. Santangelo, *Soft Matter* **8**, 2375 (2012).
11. M. A. Dias, L. H. Dudte, L. Mahadevan, C. D. Santangelo, *Phys. Rev. Lett.* **109**, 114301 (2012).
12. M. A. Dias, C. D. Santangelo, *EPL* **100**, 54005 (2012).
13. J. Ryu *et al.*, *Appl. Phys. Lett.* **100**, 161908 (2012).
14. M. Schenk, S. D. Guest, *Proc. Natl. Acad. Sci. U.S.A.* **110**, 3276–3281 (2013).
15. Z. Y. Wei, Z. V. Guo, L. Dudte, H. Y. Liang, L. Mahadevan, *Phys. Rev. Lett.* **110**, 215501 (2013).
16. M. Jamal *et al.*, *Adv. Healthcare Mater.* **2**, 1142–1150 (2013).
17. K. Miura, *Inst. Space Astronaut. Sci. Rep.* **618**, 1–9 (1985).
18. L. Mahadevan, S. Rica, *Science* **307**, 1740 (2005).
19. M. Ben Amar, F. Jia, *Proc. Natl. Acad. Sci. U.S.A.* **110**, 10525–10530 (2013).

20. A. E. Shyer *et al.*, *Science* **342**, 212–218 (2013).
21. E. Abbena, S. Salamon, A. Gray, *Modern Differential Geometry of Curves and Surfaces with Mathematica* (CRC Press, Boca Raton, FL, 2006).
22. T. D. Gatzke, C. M. Grimm, *Int. J. Shape Model.* **12**, 1–28 (2006).
23. L. D. Landau, E. M. Lifshitz, *Landau and Lifshitz Course of Theoretical Physics, Vol. 7: Theory of Elasticity* (Butterworth Heinemann, New Delhi, ed. 3, 1986).
24. M. Bern, B. Hayes, *Proceedings of the Symposium on Discrete Algorithms* **7**, 175–183 (1996).
25. E. Steltz, A. Mozeika, N. Rodenberg, E. Brown, H. M. Jaeger, IEEE/RSJ International Conference on Intelligent Robots and Systems (IROS), 10 to 15 October 2009, St. Louis, MO (IEEE, 2009), pp. 5672–5677.
26. T. Fukushige, S. Hata, A. Shimokohbe, *J. Microelectromech. Syst.* **14**, 243–253 (2005).
27. T. W. Ebbesen, H. Hiura, *Adv. Mater.* **7**, 582–586 (1995).
28. P. M. Chaikin, T. C. Lubensky, *Principles of Condensed Matter Physics* (Cambridge Univ. Press, Cambridge, ed. 1, 2000).
29. T. Toffoli, N. Margolus, *Physica D* **47**, 263–272 (1991).
30. E. Hawkes *et al.*, *Proc. Natl. Acad. Sci. U.S.A.* **107**, 12441–12445 (2010).
31. S. M. Felton, M. T. Tolley, C. D. Onal, D. Rus, R. J. Wood, 2013 IEEE International Conference on Robotics and Automation (ICRA), 6 to 10 May 2013, Karlsruhe, Germany (IEEE, 2013), pp. 277–282.
32. C. D. Onal, R. J. Wood, D. Rus, 2011 IEEE International Conference on Robotics and Automation (ICRA), 9 to 13 May 2011, Shanghai (IEEE, 2011), pp. 4608–4613.
33. B. An, N. Benbernou, E. D. Demaine, D. Rus, *Robotica* **29**, 87–102 (2011).

ACKNOWLEDGMENTS

The authors thank R. J. Lang, B. Johnson, B. Parker, and M. Schneider for artistic inspiration, as well as N. Bende, J. Na, M. Byun, and the Cohen laboratory for useful discussions. We also thank F. Parish for assistance with the laser cutter, as well as X. Cheng, N. Lin, and B. Leahy for their design and construction efforts on the 3D laser scanner hardware. This work was funded by the National Science Foundation through award EFRI ODISSEI-1240441 and the Graduate Research Fellowship Program, which funded J.L.S.

SUPPLEMENTARY MATERIALS

www.sciencemag.org/content/345/6197/647/suppl/DC1
Materials and Methods
Supplementary Text
Figs. S1 to S6
Movies S1 to S4
Reference (*34*)

3 March 2014; accepted 19 June 2014
10.1126/science.1252876

EARLY SOLAR SYSTEM

Stellar origin of the ^{182}Hf cosmochronometer and the presolar history of solar system matter

Maria Lugaro,[1]* Alexander Heger,[1,2,3] Dean Osrin,[1] Stephane Goriely,[4] Kai Zuber,[5] Amanda I. Karakas,[6,7] Brad K. Gibson,[8,9,10] Carolyn L. Doherty,[1] John C. Lattanzio,[1] Ulrich Ott[11]

Among the short-lived radioactive nuclei inferred to be present in the early solar system via meteoritic analyses, there are several heavier than iron whose stellar origin has been poorly understood. In particular, the abundances inferred for ^{182}Hf (half-life = 8.9 million years) and ^{129}I (half-life = 15.7 million years) are in disagreement with each other if both nuclei are produced by the rapid neutron-capture process. Here, we demonstrate that contrary to previous assumption, the slow neutron-capture process in asymptotic giant branch stars produces ^{182}Hf. This has allowed us to date the last rapid and slow neutron-capture events that contaminated the solar system material at ~100 million years and ~30 million years, respectively, before the formation of the Sun.

Radioactivity is a powerful clock for the measurement of cosmic times. It has provided us the age of Earth (*1*), the ages of old stars in the halo of our Galaxy (*2*), the age of the solar system (*3*, *4*), and a detailed chronometry of planetary growth in the early solar system (*5*). The exploitation of radioactivity to measure time scales related to the presolar history of the solar system material, however, so far has been hindered by our poor knowledge of how radioactive nuclei are produced by stars. Of particular interest are three radioactive isotopes heavier than iron: ^{107}Pd, ^{129}I, and ^{182}Hf, with half-lives of 6.5 million years (My), 15.7 My, and 8.9 My, respectively, and initial abundances (relative to a stable isotope of the same element) in the early solar system of ^{107}Pd/^{108}Pd = $5.9 \pm 2.2 \times 10^{-5}$ (*6*), ^{129}I/^{127}I = $1.19 \pm 0.20 \times 10^{-4}$ (*7*), and ^{182}Hf/^{180}Hf = $9.72 \pm 0.44 \times 10^{-5}$ (*8*). The current paradigm is that ^{129}I and ^{182}Hf are mostly produced by rapid neutron captures (the *r* process), in which the neutron density is relatively high (>10^{20} cm^{-3}), resulting in much shorter time scales for neutron capture than for β-decay (*9*). The *r* process is believed to occur in neutron star mergers or peculiar supernova environments (*10*, *11*). In addition to the *r* process, ^{107}Pd is also produced by slow neutron captures (the *s* process), in which the neutron density is relatively low (<10^{13} cm^{-3}), resulting in shorter time scales for β-decay than for neutron capture, the details depending on the β-decay rate of each unstable isotope and the local neutron density (*9*). The main site of production of the *s* process elements from Sr to Pb in the Galaxy is in asymptotic giant branch (AGB) stars (*12*), the final evolutionary phase of stars with initial mass lower than ~10 solar masses ($M_\odot$). Models of the *s* process in AGB stars have predicted marginal production of ^{182}Hf (*13*) because the β-decay rate of the unstable isotope ^{181}Hf at stellar temperatures was estimated to be much faster (*14*) than the rate of neutron capture leading to the production of ^{182}Hf (Fig. 1).

Uniform production of ^{182}Hf and ^{129}I by the *r* process in the Galaxy, however, cannot self-consistently explain their meteoritic abundances (*15*–*17*). The simplest equation for uniform production (UP) of the abundance of a radioactive isotope in the Galaxy, relative to a stable isotope of the same element produced by the same process, is given by

$$\frac{N_{\mathrm{radio}}}{N_{\mathrm{stable}}} = \frac{P_{\mathrm{radio}}}{P_{\mathrm{stable}}} \times \frac{\tau}{T} \qquad (1)$$

where N_{radio} and N_{stable} are the abundances of the radioactive and stable isotopes, respectively; $P_{\mathrm{radio}}/P_{\mathrm{stable}}$ is the ratio of their stellar production rates; τ is the mean lifetime of the radioactive isotope; and $T \sim 10^{10}$ years is the time scale of the evolution of the Galaxy. Some time during its presolar history, the solar system matter became isolated from the interstellar medium characterized by UP abundance ratios. Assuming that both ^{129}I and ^{182}Hf are primarily produced by the *r* process, one obtains inconsistent isolation times using ^{129}I/^{127}I or ^{182}Hf/^{180}Hf: 72 My or 15 My, respectively, before the solar system formation (*17*). This conundrum led Wasserburg *et al.* (*15*) to hypothesize the existence of two types of *r* process events. Another proposed solution is that the ^{107}Pd, ^{129}I, and ^{182}Hf present in the early solar system were produced by the neutron burst that occurs during core-collapse supernovae (*18*–*20*). This does not result in elemental production, but the relative isotopic abundances of each element are strongly modified because of relatively high neutron densities with values between those of the *s* and *r* processes.

[1]Monash Centre for Astrophysics (MoCA), Monash University, Clayton VIC 3800, Australia. [2]Joint Institute for Nuclear Astrophysics (JINA), 225 Nieuwland Science Hall, Department of Physics, University of Notre Dame, Notre Dame, IN 46556-5670, USA. [3]School of Physics and Astronomy, University of Minnesota, Minneapolis, MN 55455, USA. [4]Institut d'Astronomie et d'Astrophysique, Université Libre de Bruxelles, CP-226, 1050, Brussels, Belgium. [5]Institut für Kern- und Teilchenphysik, Technische Universität Dresden, 01069 Dresden, Germany. [6]Research School of Astronomy and Astrophysics, Australian National University, Canberra, ACT 2611, Australia. [7]Kavli Institute for the Physics and Mathematics of the Universe (WPI), Todai Institutes for Advanced Study, the University of Tokyo, Japan. [8]Jeremiah Horrocks Institute, University of Central Lancashire, Preston, PR1 2HE, UK. [9]Institute for Computational Astrophysics, Department of Astronomy and Physics, Saint Mary's University, Halifax, NS, BH3 3C3, Canada. [10]UK Network for Bridging Disciplines of Galactic Chemical Evolution (BRIDGCE), www.astro.keele.ac.uk/bridgce, UK. [11]Faculty of Natural Science, University of West Hungary, 9700 Szombathely, Hungary.
*Corresponding author. E-mail: maria.lugaro@monash.edu

Using origami design principles to fold reprogrammable mechanical metamaterials

Jesse L. Silverberg, Arthur A. Evans, Lauren McLeod, Ryan C. Hayward, Thomas Hull, Christian D. Santangelo and Itai Cohen

(August 7, 2014)
Science **345** (6197), 647-650. [doi: 10.1126/science.1252876]

Editor's Summary

Folding robots and metamaterials

The same principles used to make origami art can make self-assembling robots and tunable metamaterials—artificial materials engineered to have properties that may not be found in nature (see the Perspective by You). Felton *et al.* made complex self-folding robots from flat templates. Such robots could potentially be sent through a collapsed building or tunnels and then assemble themselves autonomously into their final functional form. Silverberg *et al.* created a mechanical metamaterial that was folded into a tessellated pattern of unit cells. These cells reversibly switched between soft and stiff states, causing large, controllable changes to the way the material responded to being squashed.

Science, this issue p. 644, p. 647; see also p. 623